Towards in-situ acoustic emission-based health monitoring in bio-based composites structures: Does embedment of sensors affect the mechanical behaviour of flax/epoxy laminates?

Authors: Guillem Seychal*, Emmanuel Ramasso, Patrice Le Moal, Gilles Bourbon, Xavier Gabrion, Vincent Placet

Affiliation: Univ. Bourgogne Franche-Comté, FEMTO-ST Institute, UFC/CNRS/ENSMM/UTBM, Department of Applied Mechanics, F-25000 Besançon.

Abstract: Monitoring integrity of operating structures has become a crucial need in industrial applications while motivation for more sustainable materials pushes forward the development of natural fibre composites (NFC). The complexity and variability of their failure behaviour and mechanical properties still limit the exploitation of their full potential. Acoustic Emission (AE) has shown promising results to predict remaining service life of structures, allowing identification, localisation and assessment of damages in composite materials. Thus, embedment of AE sensors could be a reliable solution for real-time Structural Health Monitoring (SHM). This paper aims to quantify the effect of embedded millimetre-sized metallic inserts mimicking sensor integration on material integrity under tensile and bending loads by means of Digital Image Correlation, AE, and infrared thermography. Results show a limited effect on monotonic tensile properties, driven by the size of the sensor, while highlighting an increase of strain and stress at failure under three-point bending. Tensile-tensile fatigue resistance is only slightly affected by the embedment of sensors, with a small increase in the S-N curve slope. Overall results suggest that the embedment of miniature sensors in NFC is possible and could be a suitable solution for damage assessment and health monitoring in such sustainable structures.

Keywords: A. Natural fibres; B. Mechanical Properties; D. Acoustic Emission; A. Smart Materials;

1. INTRODUCTION

Recent interest in continuous natural fibres reinforcement for composites has pushed forward innovation and opportunities for this new range of bio-based materials. Their mechanical properties as much as their renewability, economic aspect and potential carbon storage capacity offer promising ongoing and upcoming applications [1–3]. At the same time, needs to improve safety and failure understanding of polymer matrix composites (PMCs) structures motivate the development of different technological solutions to assess damages in composites through Structural Health Monitoring (SHM) approaches [4].

1

Among the number of existing solutions, acoustic emission (AE) is one of the most promising passive solutions, growing thanks to recent advances in signal processing and data mining. Indeed, data collected through acoustic emission technique allows to evaluate structural integrity and to identify and locate damages in real-time with a good correlation with mechanical measurements [5]. AE sensors consist generally in piezoelectric materials (usually Lead Ziconate Titanate-PZT or PolyVinyliDene Fluoride-PVDF) transducing stress waves generated by the creation and propagation of damages within the materials into electric signals. AE systems provide huge amount of data that must be collected and processed in order to identify damages. AE is generally well suited for synthetic fibre composites due to their high acoustic activity when damages initiate and propagate. De Rosa *et al.* reviewed AE techniques to assess damage in Natural Fibres Composites (NFCs) from microscale to mesoscale and highlighted the good suitability for damage assessment in NFCs too [6,7].

The relatively small size of some piezoelectric sensors and the fabrication process of PMCs allow the embedding of transducers during the composite manufacturing, leading to smart structures. Such structures could reduce material requirements and maintenance costs while increasing safety. The lack of knowledge on the long-term behaviour of NFCs could thus be counterweighted by the use of AE-based structural monitoring. The embedding of AE sensors in glass and carbon laminates is quite well documented in literature [8,9]. Indeed, integration of a metallic or ceramic part in PMC generates heterogeneity, discontinuities in the material, fibres misorientation and stress concentration that may cause a premature failure of the structure. In that sense, it is necessary to be sure that the benefits from the embedding overpass the possible negative impact on the mechanical properties induced by its intrusive nature.

Mall *et al.* studied in the late 90's the embedding of packaged PZT in quasi-isotropic carbon fibres reinforced epoxy under monotonic tensile and tensile-tensile fatigue testing with and without cut-out area at the sensor location [10–12]. The studies highlight no significant differences in the failure scenario and mechanical properties of both monotonic and fatigue loading but a change in the location and extent of delamination by reducing propagation of the delamination in the laminate.

Masmoudi *et al.* [13–15] studied the integration of PZT sensors in glass fibres/epoxy matrix composites (GFRP) under three-point bending, monotonic tension and fatigue loading. Summarised results point out that in static testing, the embedding of sensors causes a slight degradation of the mechanical properties, but does not induce any difference on the overall behaviour. In some cases (small sensors – 5mm diameter, 0.5mm thick), ultimate properties were improved compared to reference samples. The fatigue behaviour does not seem to be affected by the integration of sensors. The authors also highlighted the higher sensitivity of embedded sensors compared to surface mounted ones and the suitability of integration to effectively anticipate catastrophic failure of structures.

2

De Rosa and Sarasini [16] conducted a similar study for embedded thin PVDF chips in GFRP in monotonic tensile and three-point bending tests. Results showed a slight degradation of the ultimate strength and stiffness of about 6%. Ghezzo *et al.* [17,18] obtained similar results to De Rosa and Sarasini [16] using dummy sensors to replace real ones. This work highlighted that geometric discontinuities and matrix rich regions in the materials, caused by the chips, generate stress concentrations and premature matrix cracks during testing. In all cases, embedment of AE sensors showed good reliability and low intrusiveness, paving the way for promising applications in complex structures.

To the best of the authors knowledge, no study has been conducted on NFCs. Tripathi *et al.* [19] embedded conductive polymer nanocomposites(CNT) to measure strain in flax fibres composites but did not evaluate the effect of embedding, while showing the suitability of CNT for SHM. The present work aims to provide keys for the understanding and development of integrated structures made of natural fibres composites by studying the effect on the mechanical behaviour of the embedding of sensors, under tensile, bending and tensile-tensile fatigue solicitations monitored by AE, Digital Image Correlation (DIC) and Infrared Thermography (TIR). Targeted embedded sensors are Capacitive Micromachined Ultrasonic Tranducers (CMUT), in flax-epoxy laminates. CMUTs sensors are miniaturised AE sensors composed of an array of micromachined silicon unit membranes of different resonance frequencies, potentially increasing the bandwidth of the sensor. Fabrication and main characteristics can be found in [20]. However, while PZT sensors can be directly embedded into laminates, CMUT chips need to be packaged in a metallic shell to protect the silicon membranes and improve the signal-to-noise ratio. The insertion of CMUTs, shown in Fig. 1a) was simulated in this test campaign using dummy sensors made of brass. These dummy sensors can also simulate all types of metallic made sensors.

2. MATERIALS AND METHODS

2.1. Sample preparation

2.1.1. Reinforcements, matrix and dummy sensors

The reinforcement used is a unidirectional non-woven FlaxTape 110 manufactured by EcoTechnilin®, with an average areal weight of $110g/m^2$. The epoxy system used was composed of a partially bio-based epoxy resin containing 56% carbon from plant origin (GreenPoxy 56) and its hardener (SD 7561). The matrix was mixed with the hardener at a ratio of 0.37. Both resin and hardener were provided by SICOMIN®. Rectangular brass inserts of 10mm long by 5mm wide were embedded into some of the manufactured plates (as described in the

next section). CMUTs are currently available as 15mm diameter, 1.2mm thick circular plates. They are not yet fully mature and could evolve to a sub-millimetre thickness and a reduced rectangular shape. Geometries of the insert have been chosen considering these future perspectives of CMUTs design. Three insert thicknesses have been investigated in order to simulate different situations, from the most optimistic to the current representative size of packaged CMUTs sensors. Samples are referenced as Without Sensor (WS), Small Sensor (SS), Medium Sensor (MS) and Large Sensor (LS) for respectively pristine sample, 0.2mm, 0.5mm and 1mm thick inserts in the laminate. Tab. 1 lists the different abbreviations used to refer to specimens depending on the fibres' orientation, the testing method and the insert embedded.

2.1.2. Composite manufacturing and sample preparation

Flax-epoxy plates (300x200mm) were fabricated by hand lay-up and thermocompression in a steel mould coated by Teflon. The stacking sequence consists of 20 unidirectional plies for tensile and bending tests and 10 plies for tensile-tensile fatigue testing.

For samples with embedded insert (EIS), inserts were dipped in resin and placed between plies during the hand lay-up without cutting area, parallel to fibres as shown in Fig. 1b). Sensors are located on the symmetrical axes of the stacking sequences. For bending tests, samples have also been fabricated by offsetting inserts at 15 and 19 plies (referenced as B10, B15 and B19 respectively) as it is represented in Fig. 1 (c). Plies were impregnated with an excess of matrix of 1.3 times the mass of fibres. A specific hand lay-up process, described in [21], was followed to optimise fibre orientations and impregnation within the laminate. The process consists in pouring resin in the middle of the ply length between each ply. Once the hand lay-up is completed, the mould is closed while the two longitudinal extremities are left open to allow excess matrix to pull out. The mould is then heated up to 40°C in an AGILA® thermocompression press. Once the temperature is reached, a 3bars pressure is applied during 15 minutes. Then, the mould is heated to 60°C (curing temperature) while maintaining pressure during 1 hour. At the end of this curing cycle, heat is turned off and the mould cools down until the composite plate reaches 35°C. Post-curing was processed at 130°C during 1 hour in order to guarantee full reticulation of the epoxy matrix and relaxation of internal stresses. Samples were then laser cut using a Trotec Speedy 300® in the selected material orientations and shapes following ASTM D3039, D7264 and D3479 recommendations for tensile, bending and fatigue tests, respectively [22–24]. In order to avoid edge effect or to have a sensor too close to the edge of the specimen, the width was chosen to be 25mm in tensile tests. The average volume ratios of fibres (V_f) and voids (V_v) were then determined using the procedure adapted from ASTM D 3171-99 [25] following equations (1) and (2). All samples have been conditioned for at least 21 days at 23°C and 50%RH until

they reached equilibrium moisture content in a climatic chamber according to ASTM D5229 standards [26]. Data, shape and fibre direction are available in Tab. 2.

$$\%V_f = \frac{\frac{m_f}{\rho_f}}{\frac{m_f}{\rho_f} + \frac{m_i}{\rho_i} + \frac{m_c - m_f - m_i}{\rho_m}} \quad (1) \qquad\qquad \%V_v = 1 - \rho_c * \left(\frac{w_m}{\rho_m} + \frac{w_f}{\rho_f} + \frac{w_i}{\rho_i}\right) \quad (2)$$

with m_x being the mass, ρ_x the density and w_x the weight fraction, subscripts f, m, c, i referring to fibres, matrix, composites and insert respectively. Density of materials were provided by suppliers and fixed at 1.53 g/cm^3 for flax fibres, 1.17 g/cm^3 for epoxy matrix and 8.6 g/cm^3 for brass.

2.2. Mechanical testing

2.2.1. Monotonic tensile tests

Tensile mechanical properties have been determined using a MTS Criterion 45 tensile machine according to ASTM D3039 standard, with a gauge length of 150mm, 110mm and 100mm for the $[0]_{20}$, $[45]_{20}$ and $[90]_{20}$ samples, respectively. A 100 kN load cell was used for $[0]_{20}$ laminates while a 5 kN cell was used for $[45]_{20}$ and $[90]_{20}$ samples. The loading rate was set at 1 mm/min in order to achieve a test-to-failure greater than 1 minute and less than 10 minutes. Longitudinal strain was measured using a clip-on extensometer (50 ± 5 mm), transverse strain was measured using a knife-edge extensometer (25 ± 2.5 mm). For $[0]_{20}$ laminates, both axial and transverse strains were also determined by Finite Element Digital Image Correlation (FE-DIC). The mechanical behaviour for $[0]_{20}$ laminates is assumed to be roughly bilinear. Two apparent elastic moduli have been then evaluated by linear regression: E_1 between 0.01% and 0.15% of axial strain and E_2 between 0.4% and strain at failure. The major Poisson's ratio was calculated by linear regression between 0.01% and strain at failure. For $[90]_{20}$ and $[45]_{20}$ laminates, the apparent Young's moduli (respectively E_T and E_{45}) were calculated on the linear part of the stress strain curves between 0.01% and 0.3% axial strain. The testing setup with AE and DIC is shown in Fig. 2a).

2.2.2. Monotonic three-point bending tests

Monotonic three-point bending tests in fibre's direction were performed on a MTS Criterion 45 with a 1 kN cell. Span length was set at 115 mm. The deflection of the specimen was measured by mean of a laser displacement sensor. Tests were conducted until structural failure at a loading speed of 2 mm/min. Bending stress and strain were calculated according to the ASTM D7264 standard. The apparent bending modulus was calculated between

0.01% and 0.4% strain. Only the dummy LS sensors with different positions within the laminate were used for these bending tests and at least three samples were tested for each configuration.

2.2.3. Tensile-Tensile fatigue tests

Tensile-tensile fatigue tests in fibre's direction were performed on an Instron ElectroPulsE10000 with a 10 kN load cell. A sinusoidal waveform was applied at a 30 Hz frequency and a load ratio (R) between minimum and maximum applied stress of 0.1. This high frequency was shown recently to be well suited to accelerate fatigue tests on plant fibre composites with results similar to those obtained with the conventional 5 Hz frequency [27]. Four load levels were applied: 85%, 75%, 65%, 55% of the Ultimate Tensile Stress (UTS) of the pristine and EIS samples. Only samples without insert (FWS) and samples with medium insert (FMS) were tested in fatigue. MS was chosen to ensure a thickness ratio (sample thickness / insert thickness) similar to that used for monotonic tensile tests while providing a sample stiffness suitable for the fatigue machine capacity. At least three samples were tested for each loading level, and tests were conducted up to failure. Complete cycles were recorded at regular time intervals and the last 20 cycles were systematically recorded. The longitudinal strain was measured with a clip-on extensometer (45 ± 5 mm). Monotonic tensile tests were also conducted before fatigue on three samples of each FWS and FMS on the ElectroPulsE10000.

2.2.4. Statistical Analysis

ANOVA (Analysis of Variance) tests were performed to evaluate if the means of the measured mechanical properties of the tested batches were significantly different from each other. A single-step multiple comparison was preferred to better discriminate the influence of one of the tested features (i.e., apparent modulus 1 and 2, stress and strain at break). The confidence interval was fixed at 95%. For each test, a probability Pr was calculated. The difference between means is considered to be significant when Pr is inferior to 0.05.
A Tukey's test was used to evaluate if the means are significantly different from each other. It applies simultaneously to the set of all pairwise comparisons. Letters (a, b, c and ab) are used to report the results of the pairwise comparisons.

2.3. Real-Time monitoring and damage assessment

2.3.1. Acoustic Emission (AE)

Acoustic emission signals were recorded for all the test configurations as raw AE data streaming through a two-channel acquisition system. The acquisition system is composed of two miniature piezoelectric transducers (μ80 from Mistras Group Ltd., main resonant frequency between 250kHz and 325 kHz), preamplifiers, DC power supply and a PicoScope® 4000 to transmit signals to a computer. AE signals were acquired at 5 MHz frequency, with a 40dB preamplification. Sensors were coupled to specimens with silicon grease and installed at 130 mm,100 mm, 110 mm, 135 mm and 150 mm apart for tensile $[0]_{20}$, $[90]_{20}$, $[45]_{20}$, bending and fatigue testing respectively. Pencil Lead Breaks were performed to check the coupling before each test.

AE signals were detected and extracted using a methodology and a Matlab® code developed in the FEMTO-ST laboratory [28]. The methodology relies first on a wavelet denoising to find the onset of AE signals, followed by a feature extraction step from the raw data stream. As advised in [28], the wavelet was set to a Daubechies "dB45" (90 coefficients) with 14 levels of decomposition, and using a soft Donoho-Johnstone universal threshold with a rescaling using a level-dependent estimation of level noise. The data were also prefiltered using a 5th order high-pass filter with a band-pass frequency set at 10 kHz and a band-pass ripple equal to 0.2 dB. Hit detection parameters are PDT (Peak Definition Time) = 60 μs; HDT (Hit Definition Time) = 120 μs; HLT (Hit Lock Time) = 300 μs, with a threshold of 35dB. These parameters have been identified and used in previous studies [29]. For low stress levels in tensile-tensile fatigue tests, 5 seconds were recorded every 40 seconds in order to limit the amount of data and ease interpretation.

2.3.2. Finite Element Digital Image Correlation (FE-DIC)

DIC measurements were set to obtain full field measurements and assess a possible effect of the embedding on the strain field homogeneity during tensile test in fibre direction. A PointGrey® GrassHoper camera was used with VIC®-2D software to record images at a 1 Hz frequency. A white and black speckle pattern was laid on specimen with a spray-paint. A white layer was firstly spread on the sample, black paint was then projected to generate random pattern composed of black dots. Images were post-processed with Pyxel [30], a finite-element DIC Python software developed at the Clément Ader Institute. This method relies on minimising distance between two functions linked to reference and deformed images respectively by analysing grey level of finite element's degree of freedom (dof) environment. Since the displacement obtained for each dof is linked to a finite element mesh, deformation field can be obtained by derivation. The algorithm uses a Gauss-Newton algorithm.

The complete method and explanation can be found in [31]. The Region of Interest (ROI) is a 50mm x 25mm window placed between the two edges of the extensometer, covering the insert location in EIS samples. Finite-Element Mesh is composed of 32 elements of 6.25mm x 6.25mm size each with 8 dofs per element. The speckle pattern, DIC ROI and meshes are shown in Fig. 2a).

2.3.3. Infrared Thermography (TIR)

IR thermography was used during tensile-tensile fatigue tests to measure surface temperature in real-time and characterise the effect of the insert embedding on the self-heating mechanisms in NFCs. A MWIR3 JADE mid-wavelength from CEDIP company ranging 3-5µm spectral response, with a temperature sensitivity of 25mK at 30°C and a spatial resolution of 320x256 pixels was used. Acquisition was set between 0.1Hz and 5Hz depending on the stress level and the estimated test duration. A view of the TIR obtained field and set-up can be seen in Fig2b).

2.3.4. X-Ray Tomography

The nano-CT investigation was performed with an RX Solutions EasyTom 160. The system is equipped with an X-ray source Hamamatsu Open Type Microfocus L10711 having a maximum voltage of 160 keV and a maximum current of 200 µA. The X-ray transmission images were acquired using a detector 2530DX of 2176 x 1792 pixels^2. The tube voltage and the tube current used were 60 keV and 86 µA, respectively. The exposure time was set at 5 images/sec with an average frame reconstructed from 5 recorded images. 1440 projections were collected for each sample resulting in a time of 30 min per tomography. The entire volume was reconstructed at a full resolution with a voxel size of 20 µm corresponding to a field of view of 25 x 25 mm^2, using filtered back-projection. The data analysis was processed using VG StudioMax software. For EIS samples, only the half of the broken samples not containing the insert were analysed to avoid measurement artefacts generated by the presence of the metallic part.

3. RESULTS AND DISCUSSION

3.1. Effect of the dummy sensor embedding on the composite microstructure and constituent volume fractions

To evaluate the influence of the integration of the dummy sensors on the local microstructure of the composite, some of the samples were cut parallel (L,T') and orthogonal (T,T') to the fibres' direction at the location where

the dummy sensor was embedded as represented in Fig. 3a). The transverse cross-section was then polished to analyse the microstructure using an optical microscope. Fig. 4 b) and c) presents two representative cross sections in the (L,T') and (T,T') planes, respectively. Optical observations reveal a large eye-shaped matrix region of approximately 2mm long along the main axis of the insert, created by the deviation of the fibres from their original longitudinal direction. In the (T,T') cross section, the fibre deviation is less pronounced because the pattern of the reinforcement allows greater deformation of the fibres and fibre bundles in the transverse direction and a better conformation to the insert's shape. Fig. 3d) highlights the presence of microcracks (about 5μm wide 10-100 μm long) in the insert vicinity and a matrix rich layer around the insert of about 10μm thick that could be a starting point for cracks. The fibre volume fraction and void content were also calculated for each type of specimen prepared for mechanical testing. Results are summarised in Tab. 2 and the V_f, normalised using the average value of the fibre volume fraction of WS specimens, is shown in Fig. 4. A slight decrease in the V_f of about 4% is observed when dummy sensors are embedded. For the tensile specimens, the V_f decreases with the increase in the insert thickness. This is in good agreement with microstructural observations and the fabrication process. Indeed, during the thermocompression process, the insert locally plays the role of a pillar limiting the compaction of some of the reinforcement plies. The applied pressure (which is the same for all the manufactured plates whether or not they integrate dummy sensors) does not drive out the same quantity of resin from the laminate. Then, the resulting resin proportion is higher when dummy sensors are integrated. The presence of the matrix-rich region at the edge of the dummy sensors can also contribute to the minimisation of the fibre content. No significant effect on the void content is observed with the insert embedment. The variations are not significant considering the scattering in measurements for each specimen type, with values between 2.5% and 4.5%. The mean values of both volume fraction and void contents are in agreement with results found in literature [29,32,33]. The fibre volume fraction is in the upper range of available data with a relatively low scattering of the results and the void content in the lower range, attesting the good reliability of the process even in presence of an insert.

3.2. Monotonic tensile behaviour

Fig. 5 presents the stress-strain curves obtained for the composites tested in the fibres' main direction (i.e., 0°) and the longitudinal strain field obtained by FE-DIC for the $[0]_{20}$ laminates. Fig. 6 presents the stress-strain curves obtained for the two other principal directions (i.e. 90° and 45°). The values of the tensile properties determined for each specimen type are summarised in

Tab. 3. Fig. 7 gives the values of the tensile properties normalised compared to WS specimens in each direction. For WS specimens in the fibre direction, the biphasic behaviour observed is typical of UD flax composites. It includes a first phase with a quasi-linear part between 0% and 0.15% of axial strain with a quite high modulus of about 31 GPa (E_1), and a second part perfectly linear with a lower apparent modulus of approximately 25.5 GPa (E_2). The ill-point separating these two phases appears at 0.2% of strain. The failure occurs on average at a longitudinal strain of 1.34% and an ultimate stress of 340 MPa. For samples tested in the transverse direction, the tensile curve is slightly non-linear until failure, typical of an elasto-plastic behaviour. The average apparent modulus, strain and stress at failure are equal to 3.7 GPa, (E_T) 0.49% and 16.9 MPa, respectively. At 45° degree, the behaviour is almost linear with an apparent modulus of 4.9 GPa (E_{45}) in mean. The mean shear-modulus G_{LT} is then determined to be 1.8 GPa. The average values of strain and stress at failure are measured at 0.79% and 33.2 MPa, respectively. It can be noted that the curves fit each other very well, and only few variations can be observed for the ultimate tensile strength and strain. The tensile properties are comparable to those found in literature [27,32–34]. The standard deviations are less than 5% for pristine $[0]_{20}$ laminates and around 15% for $[90]_{20}$ and $[45]_{20}$ laminates. It highlights the high grade of the material and the consistency of the manufacturing process.

The overall mechanical behaviour appears to be only slightly affected by the presence of the dummy sensors. This influence is more pronounced in the fibre direction. A very small decrease of the longitudinal apparent modulus, less than 5% on average, is measured for SS and MS samples compared to WS samples. The influence of large dummy sensors (LS) is more marked, with a decrease of the apparent moduli E_1 and E_2 of approximately 12%. This can be attributed to both fibre misorientation and waviness and slightly lower V_f. In any case, ANOVA results show that the difference on the modulus is not significant, emphasising the moderate effect on the stiffness of the material. The stress and strain at failure are more likely to be affected by the presence of the insert as a decrease between 10% and 20% can be noticed and confirmed by ANOVA tests. The decrease levels are driven by the insert thickness as they are more pronounced for thicker inserts. Furthermore, no significant effect can be seen on Poisson's ratio and transverse strains. The standard deviation of EIS properties is slightly higher than for pristine ones but no detrimental scattering is measured in view of structural applications. In the other material direction (90° and 45°), a very limited effect due to the embedment is observed. The tensile stress-strain curves present a similar behaviour in all cases and no effect on apparent Young's modulus can be detected, either in 90° and 45° material directions, with no statistically significant difference. A slight decrease, of approximately 5 to 15% is measured on the stresses and strains at failure when a sensor is embedded, being more

pronounced in 45° fibre-oriented direction as supported by ANOVA results. No direct trends between the decrease level and the insert thickness can be stated in these two configurations.

Longitudinal DIC strain fields are presented in Fig. 5 at two loading levels (200MPa and just before failure) for WS, SS, MS and LS specimens tested in the fibre direction. WS samples have a homogeneous strain field with only small variations for both 200MPa and 340MPa loads. Before failure, the average strain measured from the ROI is 1.35% for the presented test with a maximum value at 1.45% and a minimum value around 1.2% at the right edge. The same observation can be made for SS samples. More pronounced heterogeneities are visible for MS and LS samples. The maximum strain values are comparable to those of the WS samples but the mean and minimum strain values are much lower. These variations reflect stress concentration zones arising after 200MPa and increasing with the load. However, these heterogeneities are not concentrated around the insert (represented in red) but distributed in the whole ROI. Hence, DIC measurements point out moderate heterogeneities in the strain field appearing before failure and amplifying with the sensor's thickness.

The failure facies of WS, SS, MS and LS samples tested in the fibre direction and tomographic pictures for WS and LS samples, are presented in Fig. 8. These observations highlight a change in the failure mode when a dummy sensor is inserted, with splitting and delamination decreasing with the increase in the dummy sensor thickness. While the WS and LS samples exhibit a step-like failure mode, the ultimate failure of all fibres in MS and LS samples is clearly located at the same height, where the sensor is positioned. Tomographic images in the (T, T') plane also highlight differences in damages and failure with numerous matrix cracks in the full gauge length of the sample, in fibre and transverse directions for WS while damages are more located in the neighbourhood of the insert in LS samples, and no matrix crack can be observed when moving away from it.

The number of AE hits and the cumulated AE energy recorded during tests are presented in Fig. 9. The overall trend is similar for the four different configurations, with a high acoustic activity at the beginning of the test followed by a less active period between 0.2 and 1.1% axial strain, preceding a significant increase in activity up to failure. However, this last part is clearly not as extended and pronounced for integrated samples as for pristine ones, while cumulative energy and total hits are comparable for all cases. This is due to the premature failure caused by the coalescence of initial cracks in the neighbourhood of the insert. Stress concentrations due to material discontinuities around the insert provoke matrix cracks and decohesion at the insert-matrix interface generating higher energy hits and earlier damages. These initials cracks can coalesce in the insert vicinity until they reached a critical size causing the failure of the specimens at a lower strain and load levels, while preserving other locations in the specimen. AE hits and cumulative energy for $[90]_{20}$ and $[45]_{20}$ samples can be found in supplementary data. For all the cases, a really low acoustic activity is recorded in the beginning of the test. The

wide majority of hits and larger energy are recorded at break, for 90° samples. The first hits occur at a lower stress level, translating prior damages in the composites, resulting in lower resistance when a dummy sensor is embedded.

From these observations, we can conclude that the main effect of the embedment of dummy sensors is observed on the ultimate strain and stress at failure for samples loaded in the fibre direction, but remains moderate in all cases. It is clear that the insert thickness drives the severity of the effect. More generally, damage mechanisms and kinetics are not impacted, but damage location is modified by the presence of dummy sensors that concentrate them in its neighbourhood, leading to fine changes in the failure mode and causing premature failure. These results obtained for NFC are similar to the observations made for GFRP [8,13,15–18] which highlight a moderate reduction of strength in $[0]_{20}$ laminates and a negligible effect for cross-ply laminates and other transverse directions, a concentration of cracks in the insert vicinity driven by the insert thickness.

3.3. Monotonic three-point bending behaviour

The influence of the integration of the dummy sensors was also evaluated on the three-point monotonic bending behaviour. It was studied using LS inserts with different positions relative to the neutral axis of the beam in the thickness of the laminate: (i) on the neutral axis (B10LS), (ii) at 15 plies (B15LS) from the compressed ply and (iii) at 19 plies (B19LS) just above the last ply. Fig. 1c) shows a schematic representation of the testing configurations. Pristine bending samples (BWS) are used to normalise the values of the measured bending properties and make comparison with the samples with the three different insert positions. Fig. 10 summarises results giving the stress-strain curves (Fig. 10a)) and the normalised mechanical properties (Fig. 10b)) obtained for the different configurations.

Tab. 4 synthesises the values of the mechanical properties measured for the tested samples. BWS samples have a mean bending modulus of 29.5GPa and an average strain and stress at failure equal to 2.03% and 270.5MPa, respectively. The bending behaviour is firstly linear of strain followed by a softening marked by an asymptotic tendency up to failure. The three BWS samples show very similar properties and low discrepancies. The mechanical properties are consistent with the supplier datasheet [35] and results from other studies [36–38].

As it can be seen, global trends emphasise a neutral and even sometimes positive effect of the integration on the bending properties. For B10LS and B15LS, stress and strain at break are 6% to 19% higher than for virgin samples. Flexural modulus is slightly increased by about 2 and 8%. The global increase of the bending properties of insert embedded samples compared to reference samples (BWS) can be attributed to the shifting of the neutral axis relieving stress in the tensed plies. Van Vuure *et al.* highlighted in a past study [39] differences between the

tensile and compressive behaviour of plant fibre composites. If compressed samples reached failure at lower stress level than in tension, they admitted greater deformations, Thus, the embedment could major the contribution of the compressed plies in bending and so enhance the ultimate properties. For B19LS samples, the bending behaviour, the flexural modulus and the stress at failure are comparable to pristine samples, only the strain at break is decreased of about 8%. This slight decrease of the ultimate strain can be linked to a stress concentration caused by the discontinuity of the last ply balancing the positive effect observed in the first two cases and thus provoking quicker failure compared to B10LS and B15LS samples. Bending modulus is not statistically affected by the presence of dummy sensors as it was already the case for the tensile modulus, while in both cases the effect is statistically significant on the stress and strain at break. However, even if the difference is significative in the case of the embedding, it can be noted that the effect is not detrimental to the behaviour of the material.

AE results obtained during monotonic three-point bending tests with hits amplitude, cumulative events and energy as a function of maximum bending strain are presented in Fig. 11. Similar trends between BWS, B10LS and B15LS samples can be observed, with few hits occurring quite regularly with increasing strain, with low amplitude and energy. A very limited increase of the AE activity at failure is observed for BWS and B10LS samples, with more energetic and higher amplitude events. However, if the global trends are comparable, it can be noted that a lower cumulative energy and number of hits are detected for B10LS and B15LS while the strain and stress at break are higher, traducing fewer major damages in the specimens before failure. AE behaviour for B19LS specimens shows a change with a clearly more important acoustic activity at earlier strain levels and higher cumulative energy after 1% bending strain, transducing earlier severe damages in the laminate. The global AE results are in agreement with the observations and hypothesis made previously as it appears that the embedment release stress concentration and thus undergoing less critical damages causing structural failure within the laminate.

3.4. Tensile-tensile fatigue behaviour

The tensile-tensile fatigue results for fibre-oriented samples with and without MS inserts are presented in Fig. 12. The S-N curves show a similar trend with a gradual decline in lifetime as the applied load increases that can be fitted by a logarithmic law (Eq. 3).

$$S_{max} = \alpha - \beta \log(N) \qquad (3)$$

With N being the number of cycles, α the ultimate tensile stress, β the slope of the Wöhler curve and S_{max} the admissible stress.

FWS samples have a β parameter equal to 17.2 which is consistent with the results of previous studies focused on similar materials [27,29,40]. FMS samples exhibit a slightly increased slope, with a β parameter equal to 19.5, reflecting a very limited effect of the dummy sensor embedment on the fatigue resistance. It is interesting to note that Berges et al.[29] found a β parameter equal to 20 for pristine samples, emphasising the suitability of the embedding and thermocompression process to obtain high-grade bio-based composites, even if they host inserts. The variations in cycle life under a same level of stress remains low, highlighting the high industrial grade of the reinforcement and composite materials. The effect of the embedment is more pronounced in NFCs (about 12%), than for graphite/epoxy [10,11] and for glass epoxy [8,13,15] for which no effect was observed in tensile-tensile fatigue testing. It is important to note that these studies were conducted on cross-ply laminates with the sensor placed between two 90° oriented plies. In this work, it is shown in monotonic tensile tests that the insert has almost no influence on the mechanical properties for 90° samples. Thus, a low influence of the insert in fatigue is also consistent for this composite orientation.

The evolution of the temperature at the surface of the samples measured using infrared thermography, as a function of fatigue life, is presented in Fig. 13a) as a function of the fraction life. The mean temperature in the ROI is slightly higher for FMS than for FWS specimens, emphasising the weak point and stress concentration created by the presence of an insert. The TIR for virgin samples shows a continuous increase for cycling at 85% and 75%UTS while a decrease and stable phase is observed for the 65%UTS and 55%UTS loading levels. This self-heating behaviour is typical from natural fibres and quite well documented in literature [27] and related to energy dissipation due to damages, frictions and cycle duration. A steady state is present in FMS at 55%UTS like in FWS but 65%UTS EIS samples follow a continuous increase. The difference in surface temperature evolution was shown by Jeannin [27] to be closely related to a test time long enough to reach a steady state and so to the test frequency. This shows that the limit between low-cycle fatigue and high-cycle fatigue is shifted by the presence of an insert, needing a lower stress level to be reached as 65%UTS for FMS specimens broke before reaching this steady state. The mean surface temperatures are globally higher for FMS samples than for FWS ones for loading levels corresponding to the same percentage of UTS, with highest temperatures located around the insert location. The mean temperature of all samples is under 70°C which remains below the onset of the glass transition temperature of the matrix. Liu et al.[41] showed that in the 20°C-70°C range of temperature, the elastic and viscoelastic properties variations are low for this material. However, as it can be seen in Fig. 13b) the maximum temperature reached by FMS samples is close to 90°C in 85%UTS and 75%UTS in the insert vicinity that could lead to a local softening of the matrix around the dummy sensor.

14

The TIR fields captured at the failure show an increase of the surface temperature at the failure initiation point. For high stress levels, the insert concentrates failure and initiates in its vicinity. However, it can be seen that for lower stress levels, the high temperature zones and initial failure are located away from the insert even if it still remains a hot zone. The failure facies of the FWS and FMS samples are very similar at their respective %UTS. For 85%UTS and 75%UTS, the failure mode is driven by fibre breakage along the transverse direction while long splitting and delamination in the whole length of the specimens happen in 65%UTS and 55%UTS samples. AE hits were also recorded for some samples, and representative results are plotted in Fig. 14. For 85% and 75% UTS, the damage mechanisms are really similar leading to a comparable number of hits, cumulated energy and acoustic activity for FWS and FMS samples. At 65%UTS, while a much lower number of hits occurs during the test for FMS specimens, the cumulative energy is comparable between pristine and embedded samples. This difference in AE behaviour highlights a change in failure mechanisms for this specific level of stress as more severe damages and self-heating appear earlier in the test, producing premature failure and leading to a lower number of hits recorded but for a comparable AE cumulated energy. For 55%UTS loads, even if less hits are recorded, the cumulated AE energy is also lower, meaning that the damages are less severe, supporting the conclusion that the influence of the insertion is less pronounced for low stress levels.

4. CONCLUSION

Natural fibres market for structural applications is experiencing an important growth due to their properties, availability and low carbon footprint [42]. However, the complex behaviour and variability of these materials hinder the ability to take full advantage of their capacity. Thus, AE-based SHM can be a way to break this actual barrier while increasing safety, sustainability and decreasing material consumptions in structures. This paper investigates the effect of embedding dummy sensors on structural integrity of flax/epoxy UD composites. Monotonic tensile and three-point bending tests were conducted for different insert thickness and position, monitored by AE and DIC to assess change in the mechanical properties, damage scenarios and failure modes. Tensile-tensile fatigue campaign was set to evaluate the effect of cyclic loadings, monitored by TIR and AE. The embedment of insert causes fibre deviations and matrix rich regions becoming preferred sites for crack initiation. The tensile properties are more affected when the material is tested in the fibre direction than in other directions. The stress and strain at failure decrease with the insert thickness, with 20% reduction in the most severe case. Heterogeneities emerge when dummy sensors are embedded. Their levels are driven by the insert thickness. AE and tomographic inspections provide knowledge to establish a failure scenario. They emphasise that the insert

does not modify the damage kinetics and modes but affects their spatial location, with damages accumulated in the insert vicinity. Under three-point bending, the presence of inserts is neutral or even sometimes beneficial on the measured properties. The tensile-tensile fatigue resistance is slightly affected by the insert. An increase of approximately 12% in the S-N curve slope is measured. Finally, overall results spotlight the feasibility of including sensors in bio-based composites. CMUT sensors were targeted as possible in-situ sensors as the operating cells are sub-millimetric sized, even if packaging is still a major issue. The multi-cell sensor could thus offer better reliability of the AE signals. These sensors should be as miniaturised as possible to limit the intrusiveness, nonetheless could open up possibilities to increase bio-based structures safety and compensate for dispersions in material properties due to agronomic, biological or environmental considerations, reducing thereby material consumptions.

Acknowledgements

References

[1] Wambua P, Ivens J, Verpoest I. Natural fibres: can they replace glass in fibre reinforced plastics? Compos Sci Technol 2003;63:1259–64. https://doi.org/10.1016/S0266-3538(03)00096-4.

[2] Bourmaud A, Beaugrand J, Shah DU, Placet V, Baley C. Towards the design of high-performance plant fibre composites. Prog Mater Sci 2018;97:347–408. https://doi.org/10.1016/j.pmatsci.2018.05.005.

[3] Yan L, Chouw N, Jayaraman K. Flax fibre and its composites – A review. Compos Part B Eng 2014;56:296–317. https://doi.org/10.1016/j.compositesb.2013.08.014.

[4] Mitsheal D. A Review of Structural Health Monitoring Techniques as Applied to Composite Structures 2017:57.

[5] Williams JH, Lee SS. Acoustic Emission Monitoring of Fiber Composite Materials and Structures. J Compos Mater 1978;12:348–70. https://doi.org/10.1177/002199837801200402.

[6] De Rosa IM, Santulli C, Sarasini F. Acoustic emission for monitoring the mechanical behaviour of natural fibre composites: A literature review. Compos Part Appl Sci Manuf 2009;40:1456–69. https://doi.org/10.1016/j.compositesa.2009.04.030.

[7] Maria I, Rosa D, Santulli C, Sarasini F. Natural Fiber Composites Monitored by Acoustic Emission n.d.

[8] Tuloup C, Harizi W, Aboura Z, Meyer Y, Khellil K, Lachat R. On the use of in-situ piezoelectric sensors for the manufacturing and structural health monitoring of polymer-matrix composites: A literature review. Compos Struct 2019;215:127–49. https://doi.org/10.1016/j.compstruct.2019.02.046.

[9] Dziendzikowski M, Kurnyta A, Dragan K, Klysz S, Leski A. In situ Barely Visible Impact Damage detection and localization for composite structures using surface mounted and embedded PZT transducers: A comparative study. Mech Syst Signal Process 2016;78:91–106. https://doi.org/10.1016/j.ymssp.2015.09.021.

[10] Mall S, Coleman JM. Monotonic and fatigue loading behavior of quasi-isotropic graphite/epoxy laminate embedded with piezoelectric sensor. Smart Mater Struct 1998;7:822–32. https://doi.org/10.1088/0964-1726/7/6/010.

[11] Mall S. Integrity of graphite/epoxy laminate embedded with piezoelectric sensor/actuator under monotonic and fatigue loads*. Smart Mater Struct 2002;11:527–33. https://doi.org/10.1088/0964-1726/11/4/307.

[12] Mall S, Hsu TL. Electromechanical fatigue behavior of graphite/epoxy laminate embedded with piezoelectric actuator n.d.:8.

[13] Masmoudi S, El Mahi A, Turki S. Effect of Piezoelectric Implant on the Structural Integrity of Composite Laminates Subjected to Tensile Loads. Appl Compos Mater 2017;24:39–54. https://doi.org/10.1007/s10443-016-9513-4.

[14] Masmoudi S, El Mahi A, Turki S. Use of piezoelectric as acoustic emission sensor for in situ monitoring of composite structures. Compos Part B Eng 2015;80:307–20. https://doi.org/10.1016/j.compositesb.2015.06.003.

[15] Masmoudi S, Mahi AE, Turki S, Guerjouma RE. Mechanical behavior and health monitoring by Acoustic Emission of unidirectional and cross-ply laminates integrated by piezoelectric implant. Appl Acoust 2014;86:118–25. https://doi.org/10.1016/j.apacoust.2014.04.011.

[16] De Rosa IM, Sarasini F. Use of PVDF as acoustic emission sensor for in situ monitoring of mechanical behaviour of glass/epoxy laminates. Polym Test 2010;29:749–58. https://doi.org/10.1016/j.polymertesting.2010.04.006.

[17] Ghezzo F, Huang Y, Nemat-Nasser S. Onset of Resin Micro-Cracks in Unidirectional Glass Fiber Laminates with Integrated SHM Sensors: Experimental Results. Struct Health Monit 2009;8:477–91. https://doi.org/10.1177/1475921709340976.

[18] Ghezzo F, Starr AF, Smith DR. Integration of Networks of Sensors and Electronics for Structural Health Monitoring of Composite Materials. Adv Civ Eng 2010;2010:1–13. https://doi.org/10.1155/2010/598458.

[19] Tripathi KM, Vincent F, Castro M, Feller JF. Flax fibers – epoxy with embedded nanocomposite sensors to design lightweight smart bio-composites. Nanocomposites 2016;2:125–34. https://doi.org/10.1080/20550324.2016.1227546.

[20] Butaud P, Le Moal P, Bourbon G, Placet V, Ramasso E, Verdin B, et al. Towards a better understanding of the CMUTs potential for SHM applications. Sens Actuators Phys 2020;313:112212. https://doi.org/10.1016/j.sna.2020.112212.

[21] Cadu T, Berges M, Sicot O, Person V, Piezel B, Van Schoors L, et al. What are the key parameters to produce a high-grade bio-based composite? Application to flax/epoxy UD laminates produced by thermocompression. Compos Part B Eng 2018;150:36–46. https://doi.org/10.1016/j.compositesb.2018.04.059.

[22] D30 Committee. Test Method for Tensile Properties of Polymer Matrix Composite Materials. ASTM International; n.d. https://doi.org/10.1520/D3039_D3039M-17.

[23] D30 Committee. Test Method for Flexural Properties of Polymer Matrix Composite Materials. ASTM International; n.d. https://doi.org/10.1520/D7264_D7264M-21.

[24] D30 Committee. Test Method for Tension-Tension Fatigue of Polymer Matrix Composite Materials. ASTM International; n.d. https://doi.org/10.1520/D3479_D3479M-19.

[25] D30 Committee. Test Methods for Constituent Content of Composite Materials. ASTM International; n.d. https://doi.org/10.1520/D3171-15.

[26] D30 Committee. Test Method for Moisture Absorption Properties and Equilibrium Conditioning of Polymer Matrix Composite Materials. ASTM International; n.d. https://doi.org/10.1520/D5229_D5229M-20.

[27] Jeannin T, Gabrion X, Ramasso E, Placet V. About the fatigue endurance of unidirectional flax-epoxy composite laminates. Compos Part B Eng 2019;165:690–701. https://doi.org/10.1016/j.compositesb.2019.02.009.

[28] Kharrat M, Ramasso E, Placet V, Boubakar ML. A signal processing approach for enhanced Acoustic Emission data analysis in high activity systems: Application to organic matrix composites. Mech Syst Signal Process 2016;70–71:1038–55. https://doi.org/10.1016/j.ymssp.2015.08.028.

[29] Berges M, Léger R, Placet V, Person V, Corn S, Gabrion X, et al. Influence of moisture uptake on the static, cyclic and dynamic behaviour of unidirectional flax fibre-reinforced epoxy laminates. Compos Part Appl Sci Manuf 2016;88:165–77. https://doi.org/10.1016/j.compositesa.2016.05.029.

[30] Jean-Charles Passieux, Rfouque. jcpassieux/pyxel: pyxel v1.0. Zenodo; 2021. https://doi.org/10.5281/ZENODO.4654018.

[31] Passieux J, Bouclier R. Classic and inverse compositional Gauss-Newton in global DIC. Int J Numer Methods Eng 2019;119:453–68. https://doi.org/10.1002/nme.6057.

[32] Liang S, Gning P-B, Guillaumat L. Quasi-static behaviour and damage assessment of flax/epoxy composites. Mater Des 2015;67:344–53. https://doi.org/10.1016/j.matdes.2014.11.048.

[33] Sala B, Gabrion X, Trivaudey F, Guicheret-Retel V, Placet V. Influence of the stress level and hygrothermal conditions on the creep/recovery behaviour of high-grade flax and hemp fibre reinforced GreenPoxy matrix composites. Compos Part Appl Sci Manuf 2021;141:106204. https://doi.org/10.1016/j.compositesa.2020.106204.

[34] Blanchard JMFA, Sobey AJ. Comparative design of E-glass and flax structures based on reliability. Compos Struct 2019;225:111037. https://doi.org/10.1016/j.compstruct.2019.111037.

[35] Ecotechnilin. Flaxtape Datasheet; 2019 n.d.

[36] Viala R, Placet V, Cogan S. Identification of the anisotropic elastic and damping properties of complex shape composite parts using an inverse method based on finite element model updating and 3D velocity fields measurements (FEMU-3DVF): Application to bio-based composite violin soundboards. Compos Part Appl Sci Manuf 2018;106:91–103. https://doi.org/10.1016/j.compositesa.2017.12.018.

[37] César dos Santos J, Ávila de Oliveira L, Panzera TH, Remillat CDL, Farrow I, Placet V, et al. Ageing of autoclaved epoxy/flax composites: Effects on water absorption, porosity and flexural behaviour. Compos Part B Eng 2020;202:108380. https://doi.org/10.1016/j.compositesb.2020.108380.

[38] Moudood A, Rahman A, Khanlou HM, Hall W, Öchsner A, Francucci G. Environmental effects on the durability and the mechanical performance of flax fiber/bio-epoxy composites. Compos Part B Eng 2019;171:284–93. https://doi.org/10.1016/j.compositesb.2019.05.032.

[39] Van Vuure AW, Baets J, Wouters K, Hendrickx K. Compressive properties of natural fibre composites. Mater Lett 2015;149:138–40. https://doi.org/10.1016/j.matlet.2015.01.158.

[40] Jeannin T, Berges M, Gabrion X, Léger R, Person V, Corn S, et al. Influence of hydrothermal ageing on the fatigue behaviour of a unidirectional flax-epoxy laminate. Compos Part B Eng 2019;174:107056. https://doi.org/10.1016/j.compositesb.2019.107056.

[41] Liu T. Multi-scale damping characterization of plant fiber composite materials n.d.:214.

[42] De Beus N, Carus M, Barth M. Natural fibres show outstandingly low CO2 footprint compared to glass and mineral fibres. Renew Carbon News 2019.

Figure captions
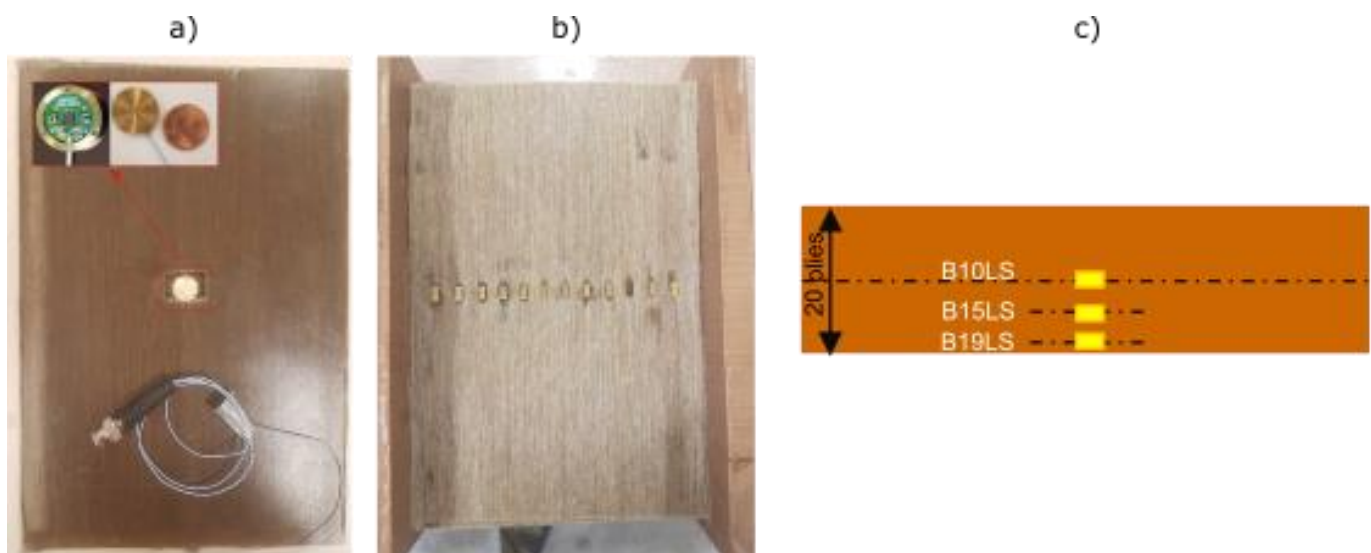
Fig. 1 a) Cured plate with embedded CMUT, pocket made by laser cutting to see the sensor b) middle ply during the hand lay-up with inserts placed c) schematic representation of the insert location in the thickness of the laminate for bending EIS specimens
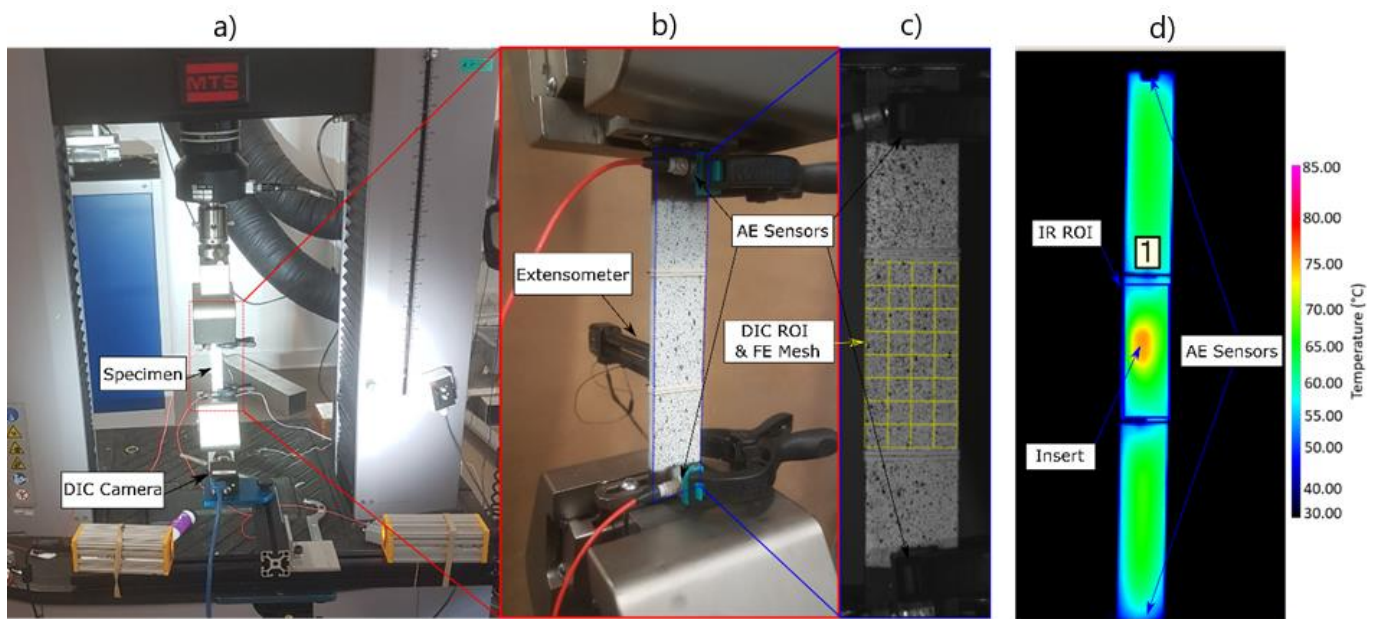
Fig. 2 a) Experimental set-up for the monotonic tensile tests with b) acoustic emission and DIC speckle and c) superposed finite element mesh. d) Thermal variation observed at the surface of the specimens by IR camera during fatigue loading
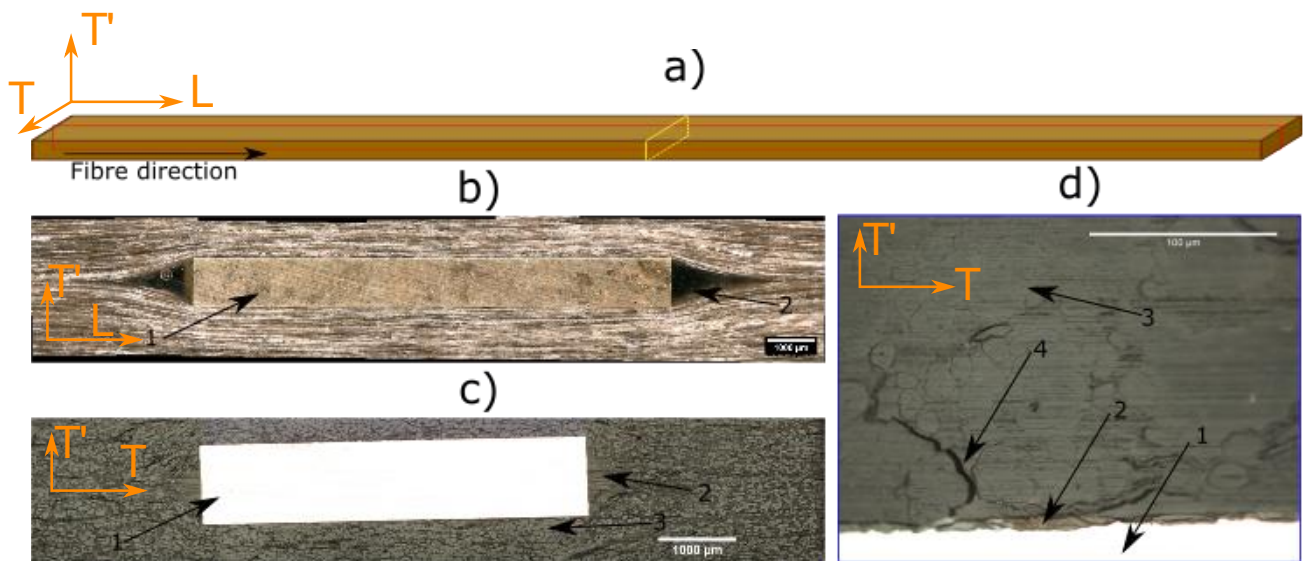
Fig. 3 Cross section of samples with embedded LS inserts. a) 3D representation of the samples and the material planes with (LT') plane in red and (TT') plane in yellow. b) (LT') cross section c) (TT') cross section d) microcracks observed in the (TT') cross-section. 1: dummy sensor, 2: matrix rich region, 3 : fibre bundles, 4: microcracks
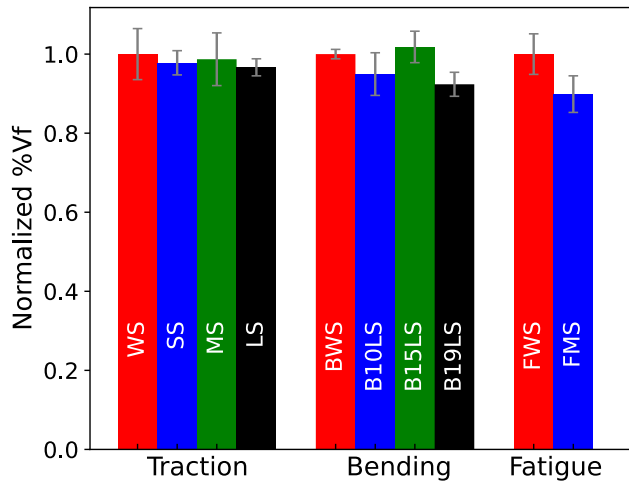
Fig. 4 Influence of the insert embedding on the fibre volume fraction. Results are normalised using the average value of the fibre volume fraction of the pristine samples (the bars represent the mean values and error bars the standard deviation).
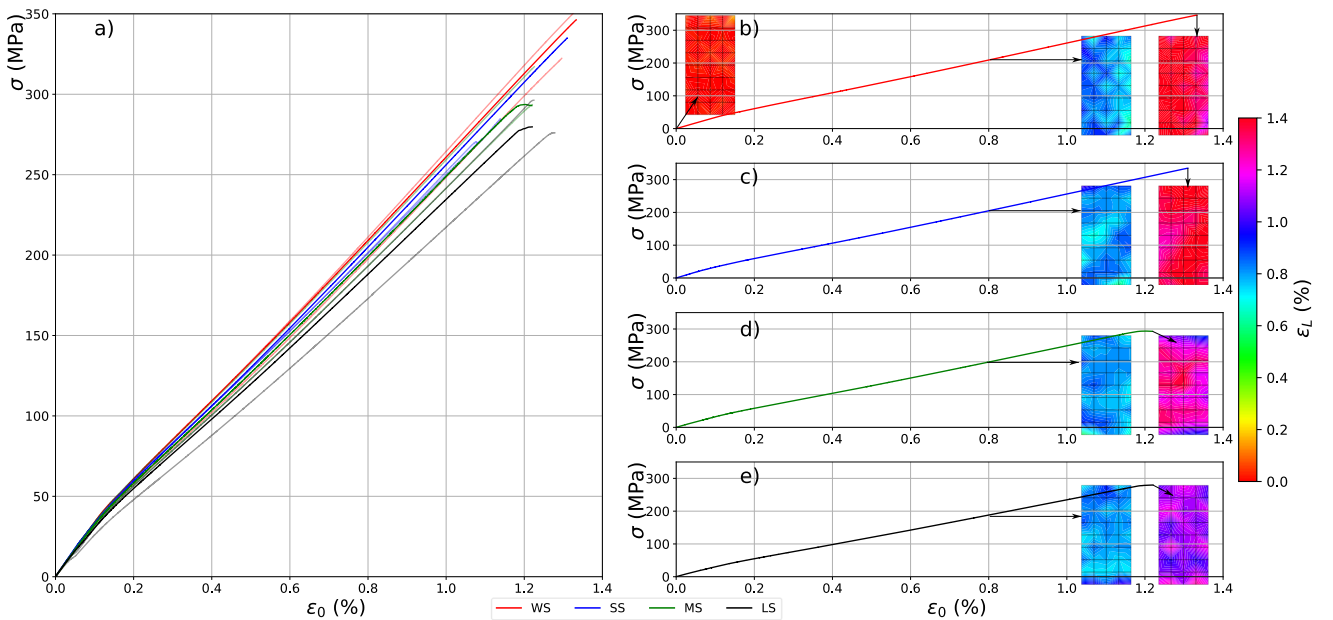
Fig. 5 Tensile stress-strain curves of pristine and embedded flax-epoxy fibres oriented laminates. a) 0° ([0]$_{20}$ samples) for all tested samples' sensor size. Representative tensile stress-strain curve in 0° direction for samples: b) Without sensor (WS), c) with Small Insert (SS), d) with Medium Insert (MS) and e) with Large Insert (LS) with longitudinal strain field obtained by DIC at 200MPa and just before failure.
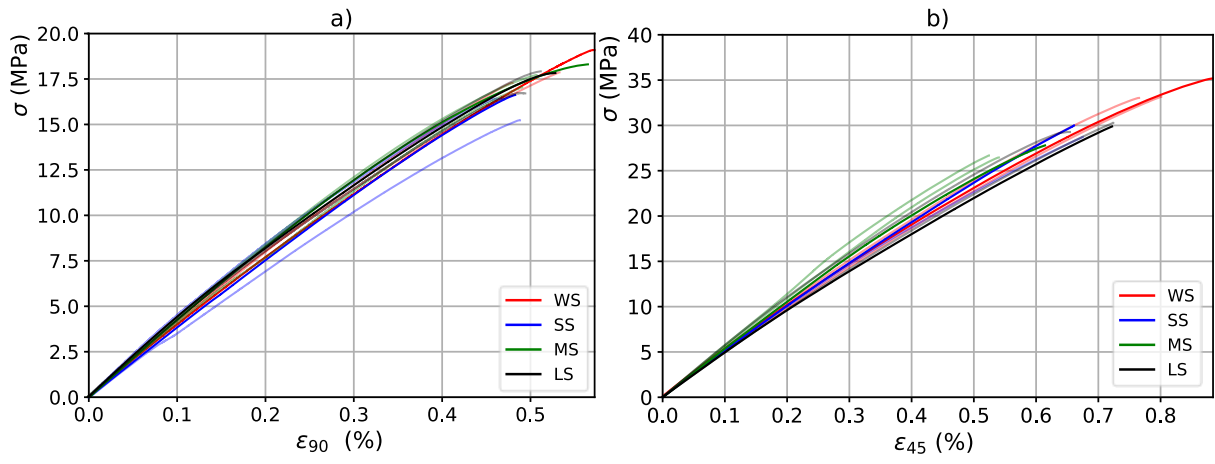
Fig. 6 Tensile stress-strain curves of pristine and embedded flax-epoxy laminates. Results for a) 90°([90]₂₀ samples) and b) 45° ([45]₂₀ samples)
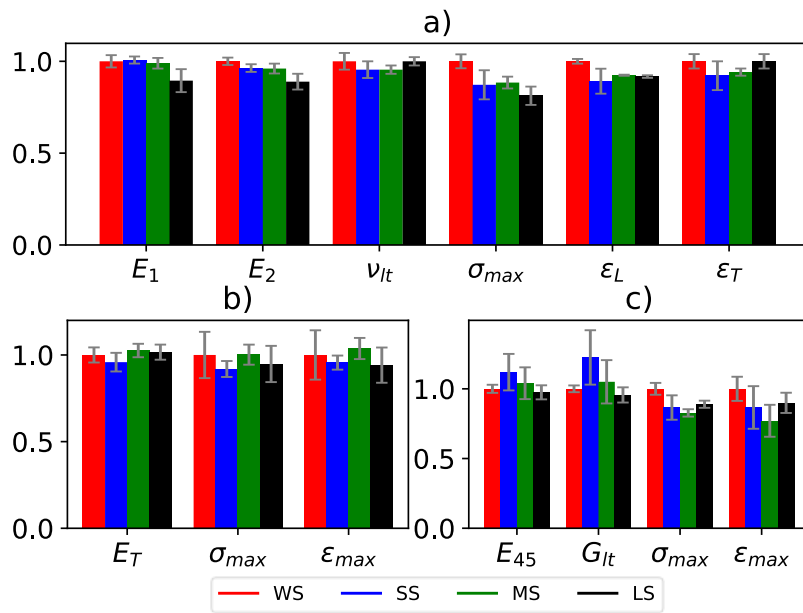
Fig. 7 Effects of the embedding of inserts on the mechanical properties in traction for a) [0]₂₀ laminates, b) [90]₂₀ laminates and c) [45]₂₀ laminates
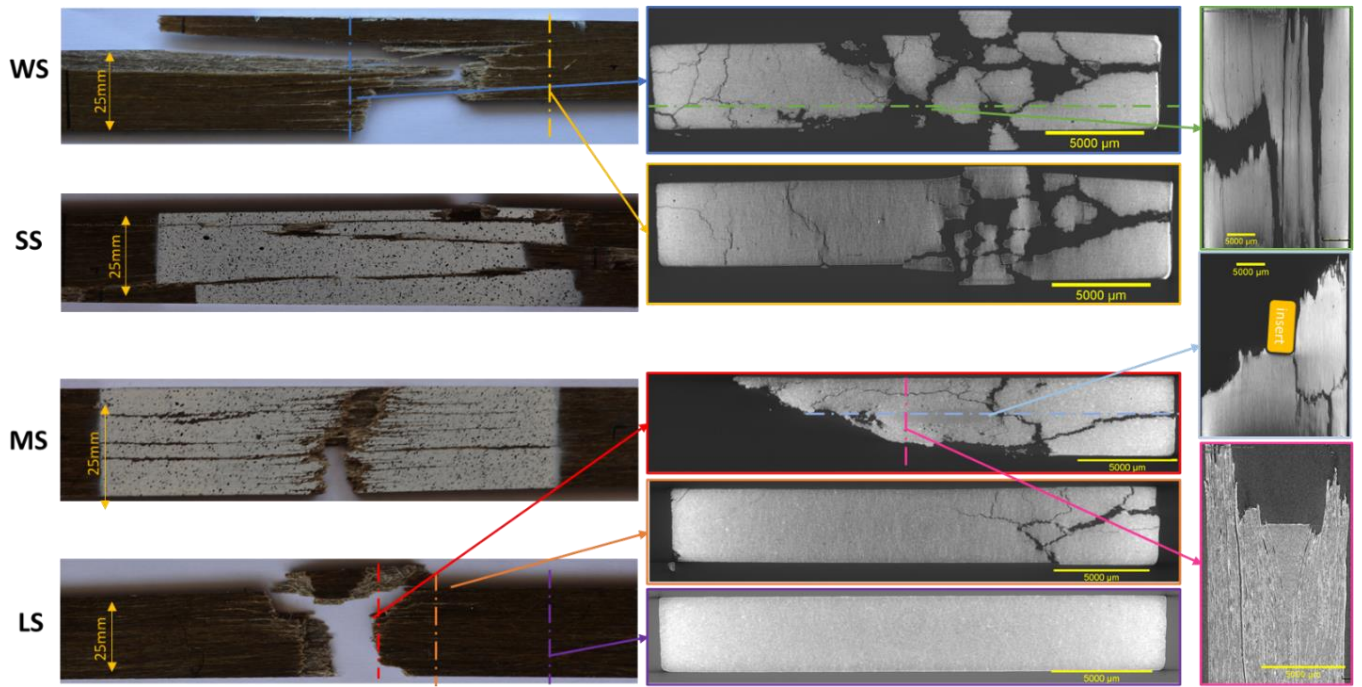
Fig. 8 Typical failure mode of the four different samples tensile tested in the fibre direction and tomographic images near the main failure zone for WS and LS samples
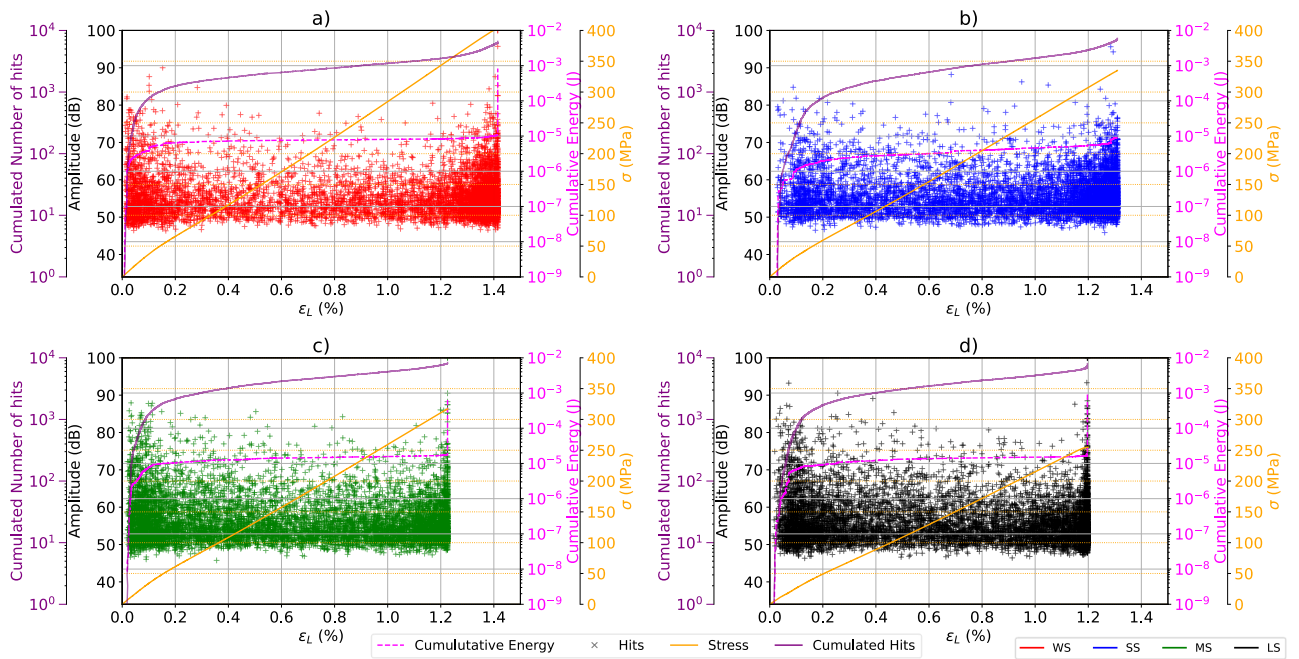
Fig. 9 AE Hits, cumulative energy and cumulative number of hits as a function of tensile strain for $[0]_{20}$ laminates. a) pristine laminate (WS), b) embedded with small sensor (SS), c) embedded with medium sensor (MS) and d) embedded with large sensor (LS)
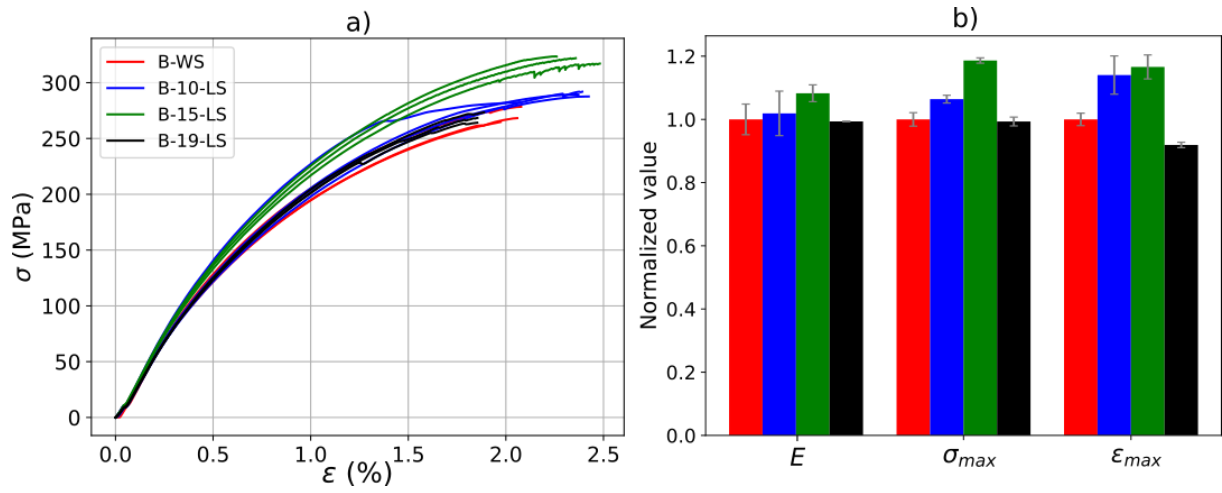
Fig. 10 a) Monotonic bending stress-strain curves for pristine and embedded samples b) normalised mechanical properties of the tested samples
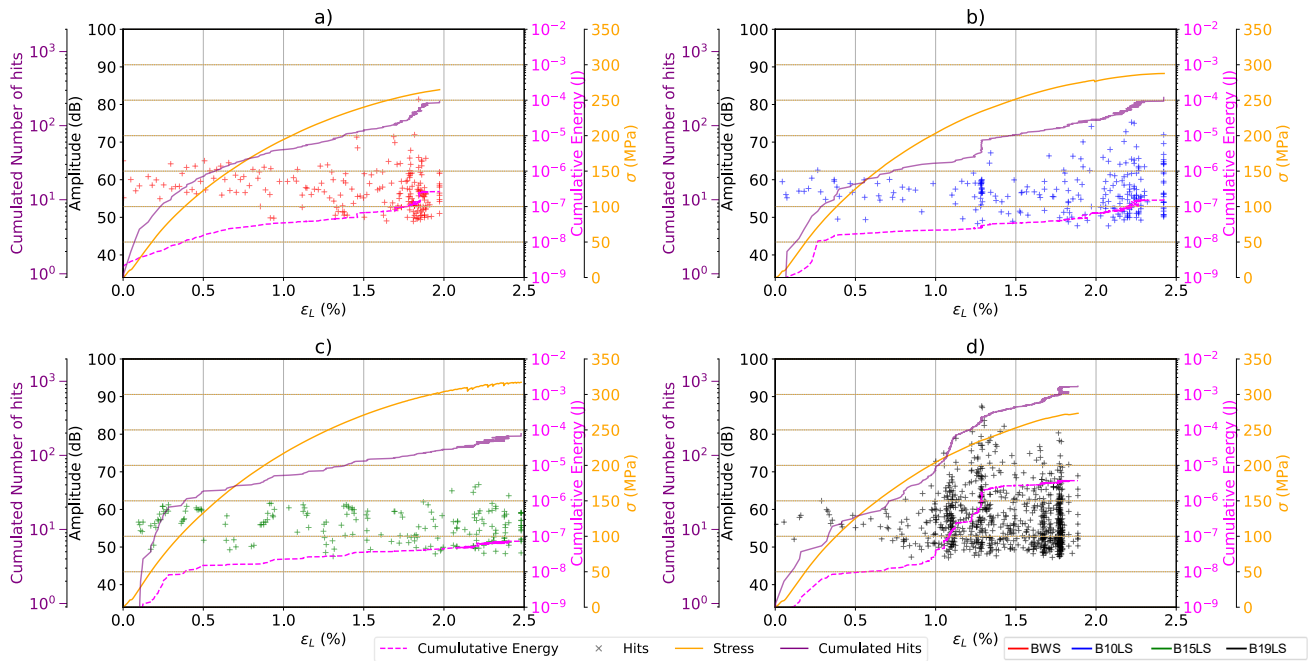
Fig. 11 Monotonic bending AE data (amplitude, cumulative energy, cumulated hits) as a function of maximum bending strain. a) BWS b) B10LS c) B15LS d) B19LS
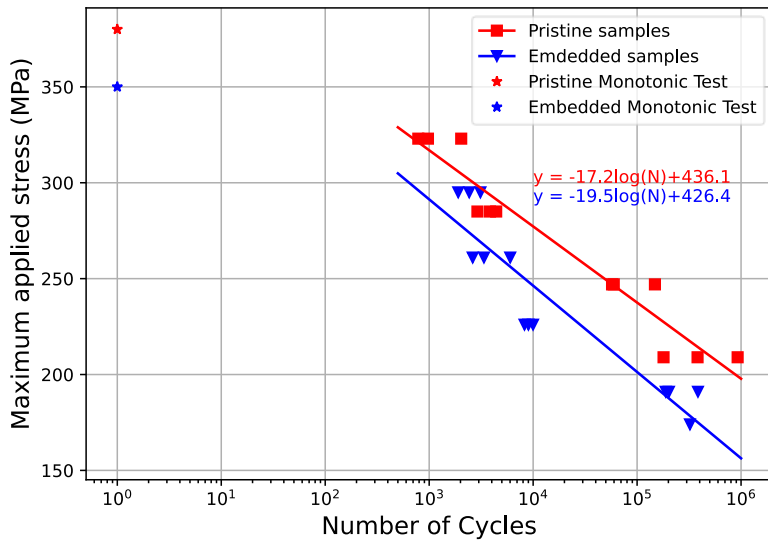
Fig. 12 S-N curve for embedded and pristine samples obtained for tensile-tensile fatigue tests.
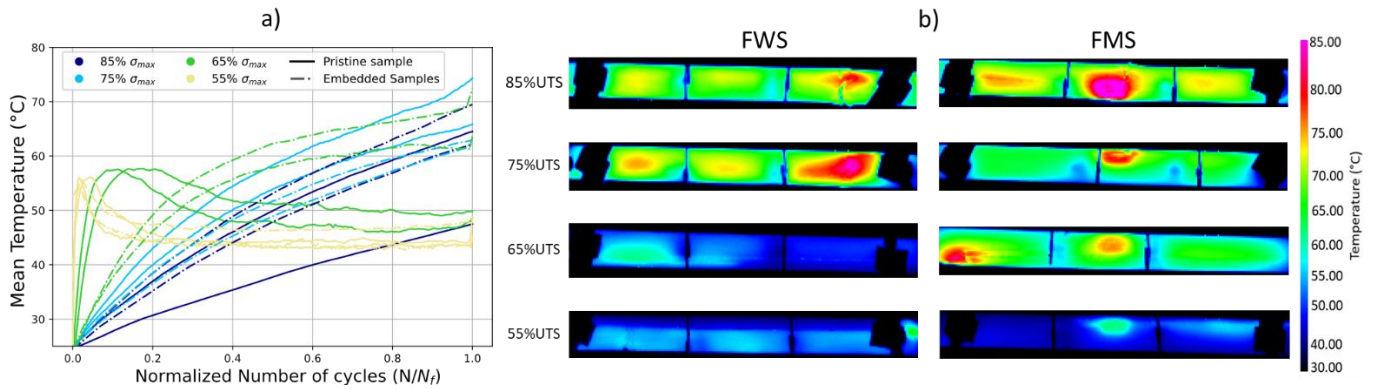
Fig. 13 a) Mean surface temperature and b) Surface temperature field obtained by infrared thermography during tensile-tensile fatigue testing for pristine (FWS) and insert embedded in samples (FMS) at 85%, 75%, 65% and 55% of the ultimate tensile stress (UTS)
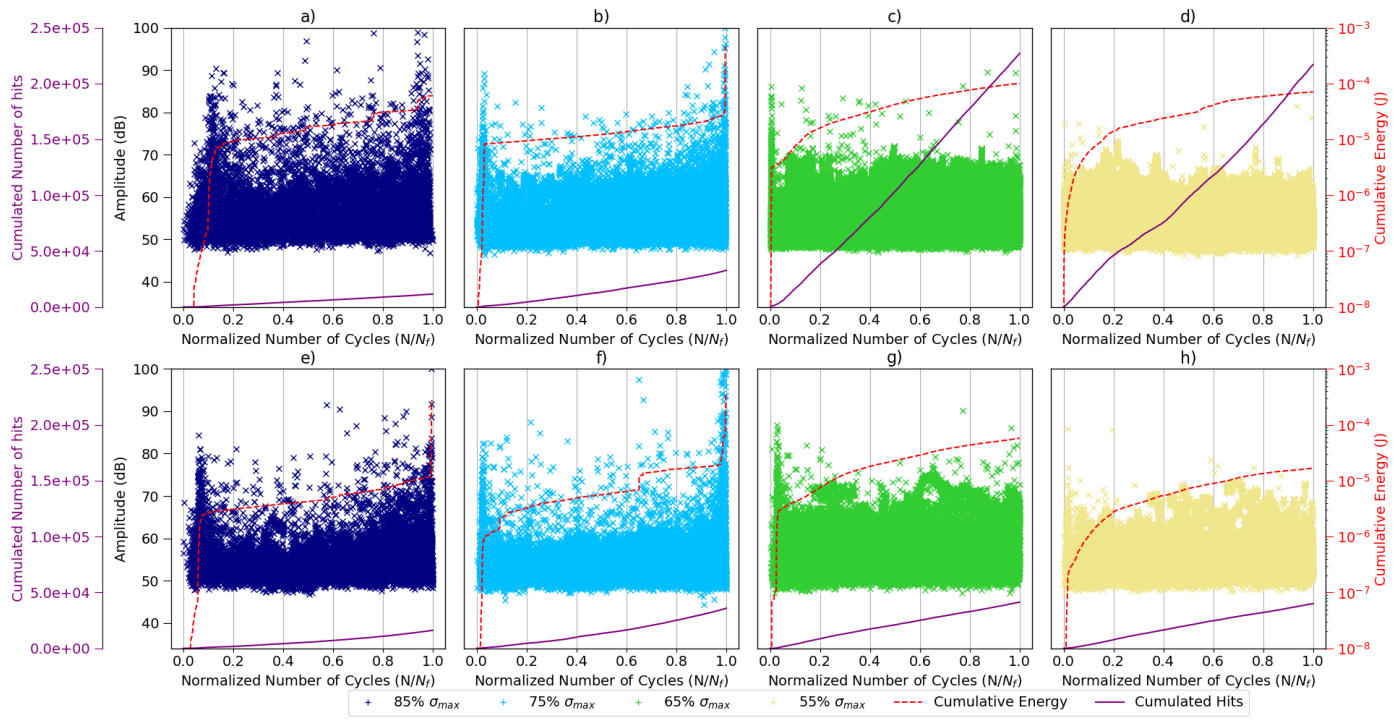
Fig. 14 AE behaviour during tensile-tensile fatigue testing for 85%UTS, 75%UTS, 65%UTS and 55%UTS (from left to right) of a-d) (FWS) pristine samples and e-h) (FMS) embedded samples

Tables

Tab. 1 Acronym used for the different tested samples

Acronym	Testing	Meaning
WS		Without Sensor
SS	all	Small Sensor (10x5x0.2mm^3)
MS		Medium Sensor (10x5x0.5mm^3)
LS		Large Sensor (10x5x1.0mm^3)
0WS		0° oriented fibres Without Sensor
0SS	Tensile Test	0° oriented fibres with Small Sensor embedded
0MS		0° oriented fibres with Medium Sensor embedded
0LS		0° oriented fibres with Large Sensor embedded
90WS		90° oriented fibres Without Sensor
90SS	Tensile Test	90° oriented fibres with Small Sensor embedded
90MS		90° oriented fibres with Medium Sensor embedded
90LS		90° oriented fibres with Large Sensor embedded
45WS		45° oriented fibres Without Sensor
45SS	Tensile Test	45° oriented fibres with Small Sensor embedded
45MS		45° oriented fibres with Medium Sensor embedded
45LS		45° oriented fibres with Large Sensor embedded
BWS		Bending specimen Without Sensor
B10LS	Three-point Bending Test	Bending specimen with Large Sensor on the 10th ply
B15LS		Bending specimen with Large Sensor on the 15th ply
B19LS		Bending specimen with Large Sensor on the 19th ply
FWS	Tensile-Tensile Fatigue Test	Fatigue specimen Without Sensor
FMS		Fatigue specimen with Medium Sensor

Tab. 2. Main features of the experimental procedure used for the manufacturing of composites (mean value ± standard deviation)

(Mechanical) Loading	Stacking sequence	Sensors	Numbers of tested samples	Sensor dimensions (mm) (Length x width x thickness)	Sensor adjacent ply	Dimensions of the samples (mm) (Length x width x thickness)	Fibre Volume Fraction (%)	Void Content (%)
Traction	[0]$_{20}$	WS	4	-	-	250x25x3.5	49.9 ± 2.8	3.1 ± 0.8
		SS	4	10x5x0.2			49.2 ± 0.4	4.2 ± 0.4
		MS	4	10x5x0.5	10		52.1 ± 3.3	4.2 ± 2.9
		LS	4	10x5x1.0			47 ± 0.5	4.5 ± 0.4
	[90]$_{20}$	WS	4	-	-	190x25x3.5	51.1 ± 1.7	3.9 ± 1.3
		SS	4	10x5x0.2			46.6 ± 0.6	3.3 ± 1.2
		MS	4	10x5x0.5	10		45 ± 0.3	1.8 ± 1.7
		LS	4	10x5x1.0			47 ± 0.9	4.2 ± 0.5
	[45]$_{20}$	WS	4	-	-	200x25x3.5	49.9 ± 0.3	3.3 ± 0.5
		SS	4	10x5x0.2			47.9 ± 1.7	2.9 ± 1.5
		MS	4	10x5x0.5	10		48.4 ± 1.6	2.9 ± 1.1
		LS	4	10x5x1.0			48.6 ± 1	4.3 ± 1.2
Bending	[0]$_{20}$	WS	3	-	-	250x20x3.5	48.1 ± 0.6	3.3 ± 0.2
		LS	3	10x5x1.0	10		44.9 ± 2.5	3.3 ± 1.3
			3	10x5x1.0	15		49 ± 1.9	2.7 ± 0.4
			3	10x5x1.0	19		44.5 ± 1.5	3.1 ± 0.7
Fatigue	[0]$_{10}$	WS	12	-	-	250x15x1.5	49.9 ± 2.6	3.1 ± 1
		MS	12	10x5x0.5	5		44.9 ± 2.3	3 ± 2.2

Tab. 3 Mechanical properties obtained in tensile test up to failure (mean value ± standard deviation) and ANOVA results

Stacking sequence		WS	SS	MS	LS	Pr >F(Model)	Significant
[0]$_{20}$	E_1 (GPa)	31.0 ± 1.0 a	31.2 ± 0.6 a	30.7 ± 0.9 a	27.7 ± 1.9 a	0.060	No
	E_2 (GPa)	25.5 ± 0.5 b	24.6 ± 0.5 ab	24.5 ± 0.7 ab	22.7 ± 1.1 a	0.024	Yes
	ν_{LT}	0.44 ± 0.02	0.42 ± 0.02	0.42 ± 0.01	0.44 ± 0.01	nd	nd
	σ_{max} (MPa)	340.9 ± 12.9 b	297.3 ± 27.0 ab	301.4 ± 11.0 ab	276.9 ± 17.0 a	0.046	Yes
	ε_L (%)	1.32 ± 0.02 a	1.18 ± 0.09 a	1.22 ± 0.01 a	1.21 ± 0.01 a	0.097	No
	ε_T (%)	0.51 ± 0.02	0.46 ± 0.04	0.48 ± 0.01	0.51 ± 0.02	nd	nd
[90]$_{20}$	E_T (GPa)	3.7 ± 0.2 a	3.6 ± 0.2 a	3.8 ± 0.2 a	3.8 ± 0.2 a	0.180	No
	σ_{max} (MPa)	16.9 ± 2.3 a	15.6 ± 0.8 a	17.0 ± 1.0 a	16.1 ± 1.8 a	0.513	No
	ε_{max} (%)	0.49 ± 0.07 a	0.47 ± 0.02 a	0.51 ± 0.03 a	0.46 ± 0.05 a	0.498	No
[45]$_{20}$	$E_{45°}$ (GPa)	4.9 ± 0.1 a	5.5 ± 0.6 a	5.1 ± 0.6 a	4.8 ± 0.3 a	0.213	No
	G_{LT} (GPa)	1.8 ± 0.1	2.3 ± 0.4	1.9 ± 0.3	1.8 ± 0.1	nd	nd
	σ_{max} (MPa)	33.2 ± 1.4 b	26.5 ± 2.9 a	27.4 ± 0.9 a	29.5 ± 0.9 ab	0.001	Yes
	ε_{max} (%)	0.79 ± 0.07 b	0.55 ± 0.12 a	0.61 ± 0.09 ab	0.71 ± 0.06 ab	0.021	Yes

Tab. 4 Flexural properties obtained in three-point bending up to failure (mean value ± standard deviation) and ANOVA results

	B-WS	B-10-LS	B-15-LS	B-19-LS	Pr >F(Model)	Significant
E (GPa)	29.53 ± 1.43 a	30.09 ± 2.12 a	31.91 ± 0.85 a	29.34 ± 0.02 a	0.288	No
σ_{max} (MPa)	270.5 ± 5.8 a	287.9 ± 3.5 b	320.9 ± 2.7 c	268.7 ± 3.8 a	<0.0001	Yes
ε_{max} (%)	2.03 ± 0.04 a	2.31 ± 0.14 b	2.37 ± 0.09 b	1.87 ± 0.02 a	0.001	Yes